Article

Not peer-reviewed version

Mechanoelectrical Effects in Composite Material as Structural Health Monitoring

Christoph Maier *, Philipp Huber, Armin Wittmann, Klaus Peter Koch, Georg Fischer

Posted Date: 25 June 2025

doi: 10.20944/preprints202506.2154.v1

Keywords: natural fiber-reinforced polymer; structural health monitoring; dynamic mechanical analysis; mechanoelectrical effect; flax fiber

Article

Mechanoelectrical Effects in Composite Material as Structural Health Monitoring

Christoph Maier [1,*], Philipp Huber [1], Armin Wittmann [1], Klaus Peter Koch [1] and Georg Fischer [2]

[1] Department of Engineering, Trier University of Applied Sciences, Schneidershof 1, Trier, 54293, Rhineland-Palatinate, Germany
[2] Chair of Smart Electronics and Systems (LITES), Friedrich-Alexander-Universität Erlangen-Nuremberg, Cauerstraße 9, Erlangen, 91058, Bavaria, Germany
* ch.maier@tech.hochschule-trier.de

Abstract

Natural fiber-reinforced polymers are gaining popularity as sustainable structural materials. However, their inherent variability can limit their reliability in load-bearing applications. To address this issue, we investigate a novel structural health monitoring method that leverages mechanoelectrical effects in flax fiber-reinforced epoxy composites. In our study, a contactless capacitive coupled measurement setup records electrical polarization during fatigue testing at four load levels. The polarization signals we observed increased with increasing load levels. Additionally, changes in polarization correlate with changes in dynamic modulus, providing early indicators of potential failure. This work lays the foundation for a new type of structural health monitoring in natural fiber-reinforced polymers.

Keywords: natural fiber-reinforced polymer; structural health monitoring; dynamic mechanical analysis; mechanoelectrical effect; flax fiber

1. Introduction

Natural fiber-reinforced polymers have great potential due to their positive carbon footprint [1] and mechanical properties [2], which can be on the order of magnitude of glass fiber-reinforced polymers [3,4]. The major disadvantage of natural fiber-reinforced polymers is the fluctuation in material properties caused by the natural plant fibers [5,6] that replace synthetic fibers such as glass fiber or carbon fiber in the composite. Therefore, structural health monitoring systems [7] are essential for using natural fiber-reinforced polymers in load-bearing structures.
The authors recently published a paper presenting a dynamic deformation sensor for natural fiber-reinforced polymers [8]. This work goes beyond the earlier published work in [8] by evaluating the mechanoelectric effect as a structural health monitoring system.

Several methods can be used to evaluate the service life of fiber-reinforced polymers in a non-destructive manner [9]. Baron et al., for example, have developed a system for natural fiber-reinforced polymers based on an embedded copper conductor. This sensor system uses high-frequency alternating currents to estimate the boundary layer condition between the conductor and the composite. Afterward, the condition and the composite's remaining service life can then be estimated [10,11], but the correlation between the boundary layer and the remaining service life of the composite requires further research. Additionally, larger conductor diameters result in a more significant effect size, but may negatively impact the composite material properties. Another approach uses electrical conductivity by incorporating conductive filler materials, such as carbon nanotubes (CNTs), into the liquid resin [12,13]. When damage occurs within the composite, the conductivity changes upon the application of voltage. This method allows for the detection of fiber breaks, matrix cracks, and delamination. However, it has a significant drawback: the manufacturing of the composite can be significantly complicated by the amount of filler used [13]. The nanofillers tend to agglomerate, necessitating the

 doi:10.20944/preprints202506.2154.v1

use of special mixing methods to achieve a uniform dispersion [13]. Additionally, the viscosity of the matrix increases with the amount of filler, leading to higher porosity and, consequently, a decrease in compressive strength [14]. To address this issue, a complex degassing procedure would be required for matrices with high filler content [14]. Recording the acoustic emissions of composite materials using piezoelectric acoustic sensors is also feasible, which typically involves multiple sensors that can detect acoustic events and ascertain the location of damage based on wave velocity [15,16]. These acoustic sensors must be integrated into the material to achieve an optimal signal-to-noise ratio [17]. However, this integration presents a challenge, as the sensors can affect the mechanical properties of the composite [18]. Additionally, the ceramic structure of piezoelectric sensors makes them susceptible to damage under strain [19]. Techniques that utilize optical measurements include digital image correlation [20], X-ray radiography [21], and shearography [22]. However, these methods frequently face challenges due to high equipment costs and their sensitivity to environmental factors such as lighting, vibrations, and rigid body motion [23,24].

In contrast to the previously discussed methods, our approach leverages mechanoelectric effects within the composite material, which can be measured using capacitive coupling techniques. This method enables a comprehensive characterization of the overall condition of the composite material. Furthermore, our method provides the additional benefit of flexible sensor deployment, as sensors, in the form of conductive plates or foils, can be integrated into the composite. As a result, it enables quantifying changes in the material's mechanical properties through electrical signals, offering valuable insights into the composite's condition in an easy, cheap, and safe way. This work serves as the initial proof of a phenomenon that paves the way for new methods of monitoring the service life of composite materials. Additionally, we wanted to gain a deeper understanding on the mechanoelectrical effect more precisely.

2. Materials and Methods

2.1. Manufacturing of Flax Fiber-Reinforced Polymer Samples

Compression molding was selected as the manufacturing process for the natural fiber-reinforced polymers, as the material properties in terms of stiffness and strength are superior or identical to most other processes such as hand lay-up, resin transfer molding or vacuum infusion [25,26]. The samples were produced using a heated press with plates measuring 150 × 200 mm^2, limited by the dimensions of the heating surface. Each laminate consisted of 8 layers of unidirectional flax (BComp ampliTex [27], each fiber is itself twisted from individual fibers [28,29]), infused with Entropy Resins 305 epoxy [30], and combined with Entropy Resins CPF-fast hardener [31]. The weights of the flax fibers and the epoxy resin were measured using a Kern digital scale [32] (0.01 g tolerance) prior to manufacturing. During the assembly process, epoxy resin was applied to the flax layers after every two layers to ensure uniform distribution [33]. The curing process was conducted at a temperature of 82°C [30,31] under a pressure of 13.6 bar, which led in our previous tests to the best material properties and a sample thickness of 2.35±0.2 mm. The completed composite panel underwent milling procedures using a milling machine to produce 170 x 17 mm^2 samples. These dimensions are taken from DIN EN ISO 574-4 [34] and are compatible with other common static and dynamic standards such as ISO 13003 [35], ASTM D3039 [36], and ASTM 3479 [37]. The fiber volume fraction of all samples was 50%±2% according to the calculation method presented by Roe et al. [38]. Subsequently, the samples were sealed under vacuum conditions at room temperature until further tests began to mitigate environmental influences, such as moisture absorption [39].

2.2. Dynamic Investigation of the Composite Material

A fatigue test was performed on the Instron 8872 Servohydraulic fatigue testing system using a tension-tension setup to measure the mechanical and mechanoelectrical effects. The fatigue testing system is equipped with hydraulic clamping jaws. The fatigue test follows standard testing procedures as defined in ASTM D3479 [37], applying load levels of 50%, 60%, 70%, and 80% of the Ultimate Tensile

 doi:10.20944/preprints202506.2154.v1

Strength (UTS), with an r-ratio of 0.1, consistent with other studies [25,40]. Prior to the fatigue test, tensile tests were conducted according to ASTM 3039 [36] to determine stress levels, resulting in a UTS of 360 MPa. The maximum and minimum stress levels of a sinusoidal load correspond to

$$\sigma_{max} = \alpha \cdot UTS \tag{1}$$

$$\sigma_{min} = R \cdot \sigma_{max} = R \cdot \alpha \cdot UTS \tag{2}$$

where UTS refers to the Ultimate Tensile Strength of the material, α is the load level as a fraction of UTS, R is the r-ratio, σ_{max} is the maximum stress and σ_{min} is the minimum stress, which was used during the test. To accelerate the general fatigue test, using the highest possible frequency, similar to [40,41] is important. However, because the temperature increase depends on both the load level and the frequency [42,43], it is not feasible to use an arbitrarily high frequency. The frequency at different load levels was chosen so the temperature would not exceed 50°C [43]. One drawback of this approach is that the elevated temperature can accelerate the aging process even at lower loads [43–45]. Consequently, it can be concluded that the number of cycles performed at lower load levels and higher frequencies should be considered conservative. In other words, the samples would withstand at least this number of cycles at the same load level but with a lower frequency. Preliminary tests have determined the following frequencies: 5 Hz for 80% and 70% of the UTS and 10 Hz and 20 Hz for 60% and 50% UTS, respectively. For the mechanical evaluation, we selected the normalized dynamic modulus E^*, $tan\delta$, and displacement as key parameters. The normalized dynamic modulus is commonly referenced in the literature [41,46–48] and serves as a preferred method for investigating the viscoelastic behavior and stiffness characteristics of materials under cyclic loading. The $tan\delta$, defined as the loss factor, represents the ratio of the loss modulus to the storage modulus [37]. Flax fiber-reinforced polymers typically exhibit a higher $tan\delta$ compared to other composites [49–51], which suggests a relatively greater loss modulus in relation to the storage modulus. This characteristic leads to increased damping and heat build-up during dynamic loading of natural fiber-reinforced polymers [52,53]. The displacement observed throughout load cycles enables the assessment of time-dependent deformation behavior, allowing for the early detection of damage mechanisms within the material. Notably, abrupt changes in length amplitude serve as indicators of critical conditions, signaling the potential onset of crack formation or structural failure. A total of 12 tests were conducted per load level, resulting in a total of 48 tests. Two datasets from every load level were chosen to illustrate the mechanical and electrical behavior. The total test duration was 3 months for all 48 tests.

2.3. Electrical Measurement Setup

The electrical response of the specimen was measured by utilizing a plate capacitor setup. The polarization resulting from mechanical deformation in the material leads to charge displacement inside the material, which can be observed as current flowing from one electrode to the other, which is then measured. When demonstrating the sensor principle in [8], an embedded copper conductor represented one electrode and the surrounding test setup the other. However, this approach presents several significant drawbacks, primarily the risk of conductor detachment from the composite, which cannot be ignored. The resulting microphonic effects [54] from this setup may interfere with other phenomena, such as piezoelectric or flexoelectric effects, complicating the accurate identification of the specific effect being measured. Furthermore, should the integrated conductor become detached from the composite material during dynamic mechanical analysis, it could introduce additional unforeseen effects. As a result, this setup might be more indicative of the boundary layer between the conductor and the composite (cf. [11]), rather than the composite itself. Consequently, utilizing an integrated conductor is not advisable at this stage of the research.

Instead, we implemented a contactless measurement method where no microphonic effect or triboelectric effect can occur due to an integrated conductor (cf. Figure 1a and b). This method offers the significant advantage of not impacting the composite material, thereby avoiding the introduction of additional mechanoelectric effects. Two electrodes were placed on opposite sides of the sample,

 doi:10.20944/preprints202506.2154.v1

creating a capacitor with three stacked dielectrics: air, NFRP, air. One electrode was connected to the central conductor of a triaxial cable, while the other was connected to the inner shielding of the same cable. To minimize noise, it was crucial to employ additional shielding around the test setup in the form of a Faraday cage, which was also connected to the inner shielding of the triaxial cable. The inner and outer shields were short-circuited by a triaxial to biaxal connector. This triaxial cable was connected to a high-resolution ammeter (Keysight B2987B). The following current range was chosen: 200 pA, with a resolution of 100 aA.

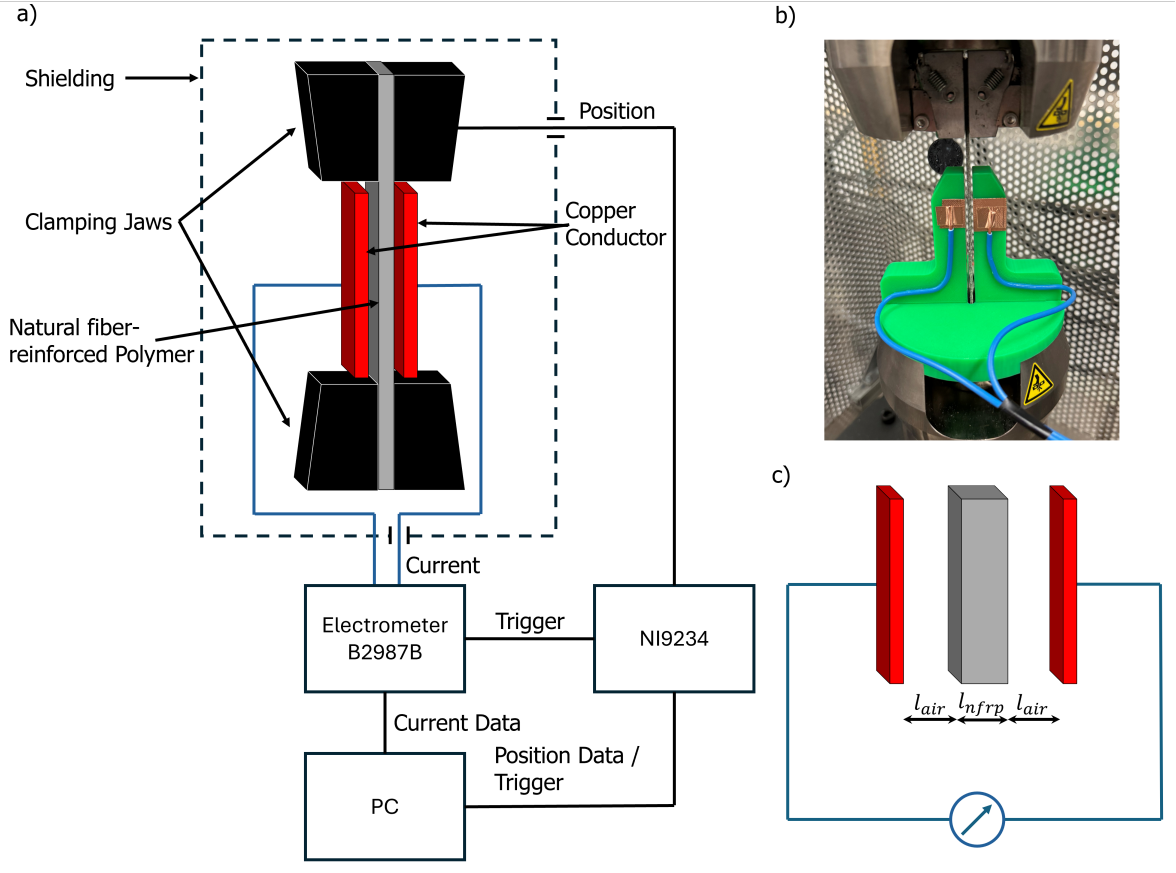

Figure 1. Experimental setup for measuring the electrical response of natural fiber-reinforced polymer composites under mechanical loading. a) Schematic Representation of the measurement setup of the natural fiber-reinforced polymer specimen (grey) in the tensile test (black) with contactless measurement using a copper electrode (red). The measuring instruments and the connection are also shown. b) Illustration of the actual test setup. The specimen are clamped in the dynamic tensile testing machine. The electrodes are attached to the side with an additional structure. c.) Simplified electrical setup with natural fiber-reinforced polymer (gray) and electrodes (red).

The lower clamping jaws of the fatigue testing machine were fixed, while the upper jaw was connected to the actuator of the fatigue testing machine. The actuator's position was transmitted as a voltage signal to a data acquisition card (DAQ, NI-9234) with a sampling rate of 8533.33 Sa/s. The ammeter sent a trigger signal to the measurement card, synchronizing the position data and electrical signals at the beginning of each measurement. The ammeter can store a maximum of 100,000 measurement points, making the measurement of the complete test at once impossible. With a sampling rate of 1500 Sa/s, one measurement period equals 1 minute. To reduce the evaluation workload, at the beginning of the study, it was chosen to increase the pause duration after each measurement (no pause at the test beginning, 2 minutes after 30 measurements, and 15 minutes after 40 measurements). Since significant changes in the signaldid not occur at the beginning of each test, as expected, the sampling rate was decreased to 750 Sa/s, and no pause between measurements for the load levels of 50% and 60% UTS, resulting in only a few seconds interruption between measurements due to

 doi:10.20944/preprints202506.2154.v1

data transmission and resetting of the ammeter. As a result, sudden events may not be recorded for specimen reaching a higher end-of-life of the load levels of 70% and 80% UTS. After each measurement, the position and electrical data are transmitted to the computer. The mechanical parameters recorded by the Instron Servohydraulic testing system can be synchronized with the measurement data of the electrical measurement setup using the position data.

2.4. Derivation of Composite Material Polarization

To enhance the comparability of future studies, the material's polarization was calculated, which is common when working with mechanoelectrical effects [55–57], rather than relying on the measured current, as demonstrated in our previous work [8]. Therefore, the theoretically measured voltage between the two electrodes is calculated first, which can be derived from the line integral of the electric field [58]:

$$V_{meas} = \int_a^b \mathbf{E} \cdot \mathbf{dl} \tag{3}$$

where $\mathbf{E}$ is the electric field vector and dl is the infinitesimal line element along the path from point a to point b. Only the component of the electric field that acts in the direction of the surface is taken into account. The total voltage can be expressed as (cf. 1c):

$$V_{meas} = E_{air} l_{air} + E_{nfrp} l_{nfrp} + E_{air} l_{air} \tag{4}$$

$$V_{meas} = 2E_{air} l_{air} + E_{nfrp} l_{nfrp} \tag{5}$$

where E_{air} and E_{nfrp} are the electric fields in air and the composite material, respectively, while l_{air} and l_{nfrp} represent the air gap between the electrode and the composite surface, and the thickness of the composite, respectively. The electric field in air, E_{air}, is determined using the electric displacement field [58]:

$$E_{air} = \frac{D_{air}}{\varepsilon_{air}\varepsilon_0} \tag{6}$$

where D_{air} is the displacement field in air, ε_{air} is the air permittivity, and ε_0 is the vacuum permittivity. The relative permittivity of air is assumed to be one. For the composite material, the electric field E_{nfrp} is defined in terms of both the displacement field and the material's polarization [58]:

$$E_{nfrp} = \frac{D_{nfrp} - P_{nfrp}}{\varepsilon_0 \varepsilon_r} \tag{7}$$

where D_{nfrp} is the displacement field in the composite, P_{nfrp} represents its polarization, and ε_r is its relative permittivity. Since no free surface charges are present as a decharging procedure is performed upfront (see next section), Gauss's law states that:

$$D_{nfrp} = D_{air} = D \tag{8}$$

Substituting this into the voltage equation gives:

$$V_{meas} = 2\frac{D}{\varepsilon_0} l_{air} + \frac{D - P_{nfrp}}{\varepsilon_0 \varepsilon_r} l_{nfrp} \tag{9}$$

Under short-circuit conditions, where $V_{meas} = 0$, we solve for the polarization P_{nfrp}:

$$P_{nfrp} = D\left(2\varepsilon_r \frac{l_{air}}{l_{nfrp}} + 1\right) \tag{10}$$

 doi:10.20944/preprints202506.2154.v1

Since the system is modeled as a parallel-plate capacitor (neglecting edge effects), the displacement field D is given by:

$$D = \frac{Q_{meas}}{A} = \frac{\int_0^t I_{meas} dt}{A} \tag{11}$$

where Q_{meas} is the measured charge, I_{meas} is the measured current, and A is the electrode surface area. Substituting this into the polarization equation yields:

$$P_{nfrp} = \frac{\int_{t_0}^t I_{meas} dt}{A} \left(2\varepsilon_r \frac{l_{air}}{l_{nfrp}} + 1 \right) \tag{12}$$

For the measurements, the area of the electrodes A, the distance of the electrode to the material l_{air} and the thickness of the material l_{nfrp} is given by the geometry. In the following, it is assumed that the variable l_{nfrp} remains constant. With a Poisson's ratio ν_{12} of approximately 0.4 [59,60] and a maximum mean displacement of approximately 2 mm, the change in thickness corresponds to about 11.05 μm based on our sample geometry. All that remains is the measured current I_{meas} and the relative permittivity ε_r. Several papers have studied the permittivity of flax fiber-reinforced polymers with epoxy resin [61–64]. Our experiments require frequency ranges of 5-20 Hz and temperatures between 20-40°C. However, none of these studies provides the specific combination of temperature range, manufacturing process, and frequency range required for our tests. As a result, it is necessary to conduct additional experiments, which are detailed in Appendix A.

2.5. Procedure Before the Experiment

Before every test, the specimen and surrounding test equipment (as seen in Figure 1b) have been discharged using an ionizer benchtop Panasonic ER-Q to ensure no static charges on the specimen or the test setup are responsible for the measured current signal instead of the internal effects of the specimen. After discharge, the actuator was moved with only the top clamp closed, so no mechanical force acts on the specimen, to see if any remaining static charges or disturbances from the test equipment would lead to false measurements. An example of the current signal before and after ionization can be seen in Figure 2a-b. Before ionization (a), static charges on the specimen or actuator cause a current signal according to the movement of the specimen and actuator. After ionization (b), this is reduced to a negligible minimum.

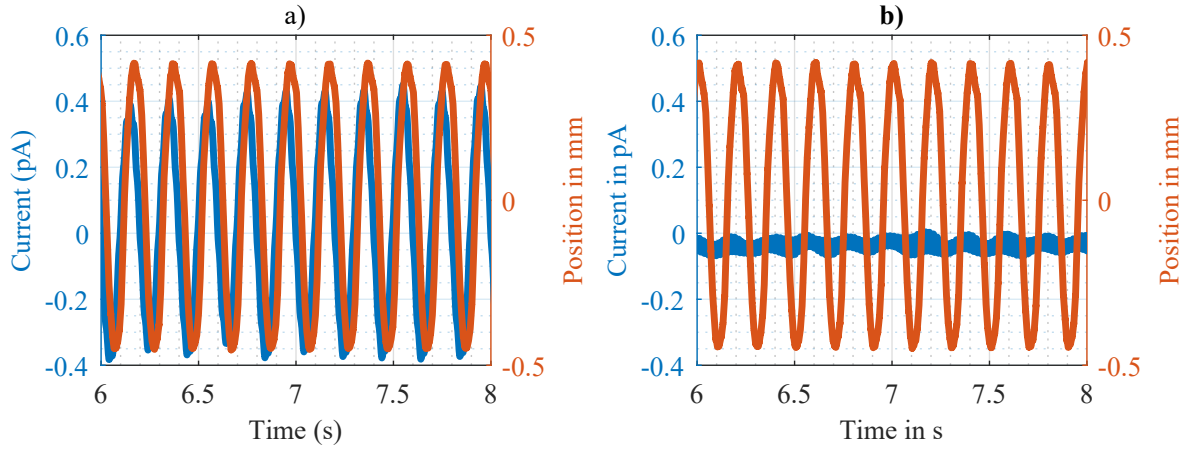

Figure 2. Measured signal with a moving actuator and open bottom clamp, so no applied force to the specimen. Before (a) and after (b) discharge of the specimen surface and the test setup surfaces surrounding the specimen.

2.6. Data Processing

The evaluation was conducted using Matlab (2023b). For the mechanical analysis, evaluation was performed automatically for each cycle using Instron WaveMatrix 2. Regarding mechanoelectrical

 doi:10.20944/preprints202506.2154.v1

analysis, polarization was calculated using equation 12. Subsequently, the norm of the resulting complex polarization was calculated. Finally, the root mean square (RMS) polarization was determined for each cycle. The cycles were normalized using the respective end-of-life cycle. Both the dynamic modulus and the polarization were normalized based on the respective values at 0.2 normalized cycles. A summary of all values used in the normalization process can be found in the Appendix C.

3. Results & Discussion

3.1. Mechanical Analysis

In the initial step, the mechanical properties of two selected datasets per load level were analyzed and compared, including E^*, $tan\delta$, and material displacement, with those documented in the literature. This comparison aims to assess the degree to which our findings align with previously reported results by other authors. Figure 3a-d illustrates the normalized dynamic modulus E^* at various load levels for two tested samples per load level. During the first approximately 1,000 cycles, all samples exhibit strain hardening, which increases the dynamic modulus by about 0.05. After this initial phase, the dynamic modulus shows a slow increase for the 70% and 80% load levels. This hardening effect is often attributed to the reorientation of cellulose fibers in the composite [42,47,65]. After the initial rise, 50% and 60% load levels experience a nearly monotonic decrease for most of the service life. Ueki et al. describe a combination of the actual stiffening effect and the softening that can be caused by damage to the fiber, which may occur during fatigue tests, explaining our observed behavior for loads of 50% and 60% [65]. Notably, the number of cycles to failure increases as the load level decreases. Detailed information on the exact number of cycles can be found in Appendix C. Just before reaching maximum service life, around 0.95, the dynamic modulus sharply declines across all load levels. Other authors have observed a significant increase in acoustic emissions in this region [41,66,67]. In some instances, the samples exhibit a step-like progression in the dynamic modulus. This phenomenon has also been noted in multiple other studies [41,47,48,68]. This behavior may be due to significant damage, such as delamination or fiber breaks [42,48,69,70].

Figure 3e-h illustrates the behavior of $tan\delta$ at different load levels. In our measurements, the value of $\tan\delta$ starts at approximately 0.08 and decreases approximately linearly with the number of cycles in logarithmic scale, regardless of the applied load levels. The consistent starting values for $tan\delta$ suggest that the samples were at similar temperatures at the experiment's beginning. Alternatively, the samples could have different temperatures, but $tan\delta$ remains insensitive within this temperature range, which could also be the case because the typical sensitive temperature range of flax composites is at higher temperatures [71,72]. At lower load levels and the increasing number of maximum cycles, $tan\delta$ can fall to lower values before the break. For example, $tan\delta$ drops to about 0.05 at 80% UTS, 0.04 at 70% UTS and 0.03 for 60% and 50%. However, towards the end of the testing, $tan\delta$ sharply increases, which is attributed to material breakage.

Figure 3i-l illustrates the displacement of the tested samples. Each load level initiates at a different displacement due to the initial ramp, which elevates the sample to the appropriate mean load level. At high load levels of 80% and 70% UTS, the displacement increases rapidly after the substantial initial increase. For the 80% load level, the displacement at break reaches approximately 2000 μm, where a notable increase is observed. In contrast, for the lower load levels (60% and 50%), the displacement increases steadily after the initial significant change. Towards the end of the service life, there is a sharp increase in displacement, indicating the break of the composite. In some cases (e.g., Figure 3 in blue), the drop in the dynamic modulus results in a stronger sudden increase in displacement. This observation is not consistent with all conducted measurements (e.g., Figure 3 in red). In general, a characteristic S-curve can be recognized due to the strong change in displacement at the beginning and end of the service life [40,48]. In summary, it is notable that the observed mechanical behavior is consistent with already published results in [40,41,47,48,68].

 doi:10.20944/preprints202506.2154.v1

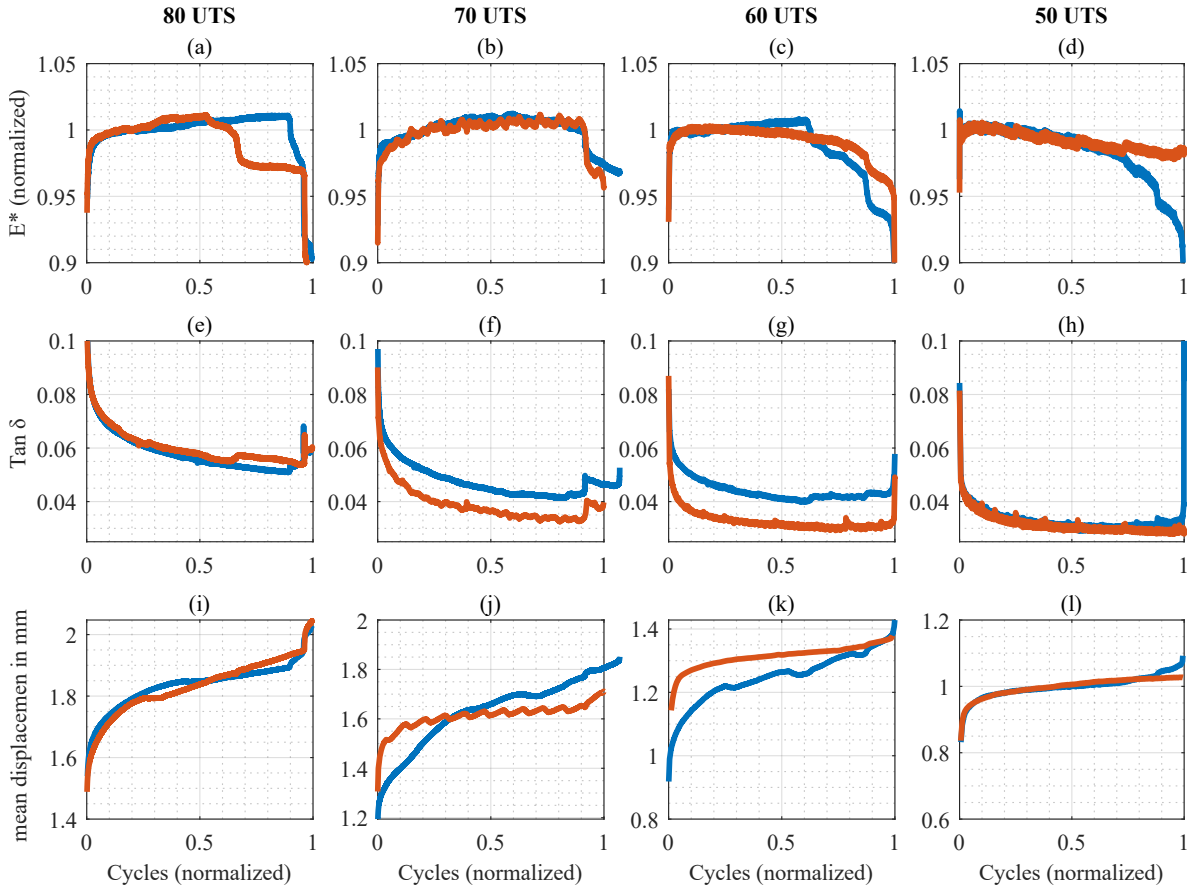

Figure 3. Results of the mechanical analysis. Normalized dynamic modulus E^* (a-d), $tan\delta$ (e-h) and displacement (i-l) in relation to normalized cycles for the load levels 80%, 70%, 60%, 50% UTS. Each load level is represented by two specimen (orange and blue lines).

3.2. Mechanoelectrial Analysis

This section will compare mechanical and electrical measurements at all load levels. First, eight samples, two per load level, will be compared over their entire service life. Figure 4 displays the relationship between normalized dynamic modulus and RMS polarization over normalized cycles for specimen tested at 80% (a and b), 70% (c and d), 60% (e and f), and 50% (g and h) UTS. For each sample, the polarization and displacement data are provided for the two points of interest (0.2 and 0.95 normalized service life). Across all load levels, the dynamic modulus typically shows a sharp increase at the onset of testing, followed by a period of gradual increase or decrease. This trend often culminates in a significant drop in dynamic modulus. In contrast, the RMS polarization exhibits a more varied behavior: it may display a slight monotonic decline, plateau, or even an initial decrease followed by a rise or fall in later stages. Nonetheless, substantial changes in RMS polarization consistently correspond to abrupt shifts in the dynamic modulus. Notably, the sample depicted in Figure 4h exhibits minimal changes in both dynamic modulus and RMS polarization, as it did not break within the test's stopping criterion of 2 million cycles. Although the waveform shape and the phase relationship between polarization and displacement remain relatively constant throughout the service life, there is a pronounced change in amplitude (see details at Markings I and II). This suggests that monitoring the signal strength alone is sufficient to detect variations in the composite material. Overall, the consistent correlation in timing and nature of the changes, particularly the synchronized signal alterations between dynamic modulus and RMS polarization, underscores the effectiveness of the electrical signal as an indicator of changes in material.

 doi:10.20944/preprints202506.2154.v1

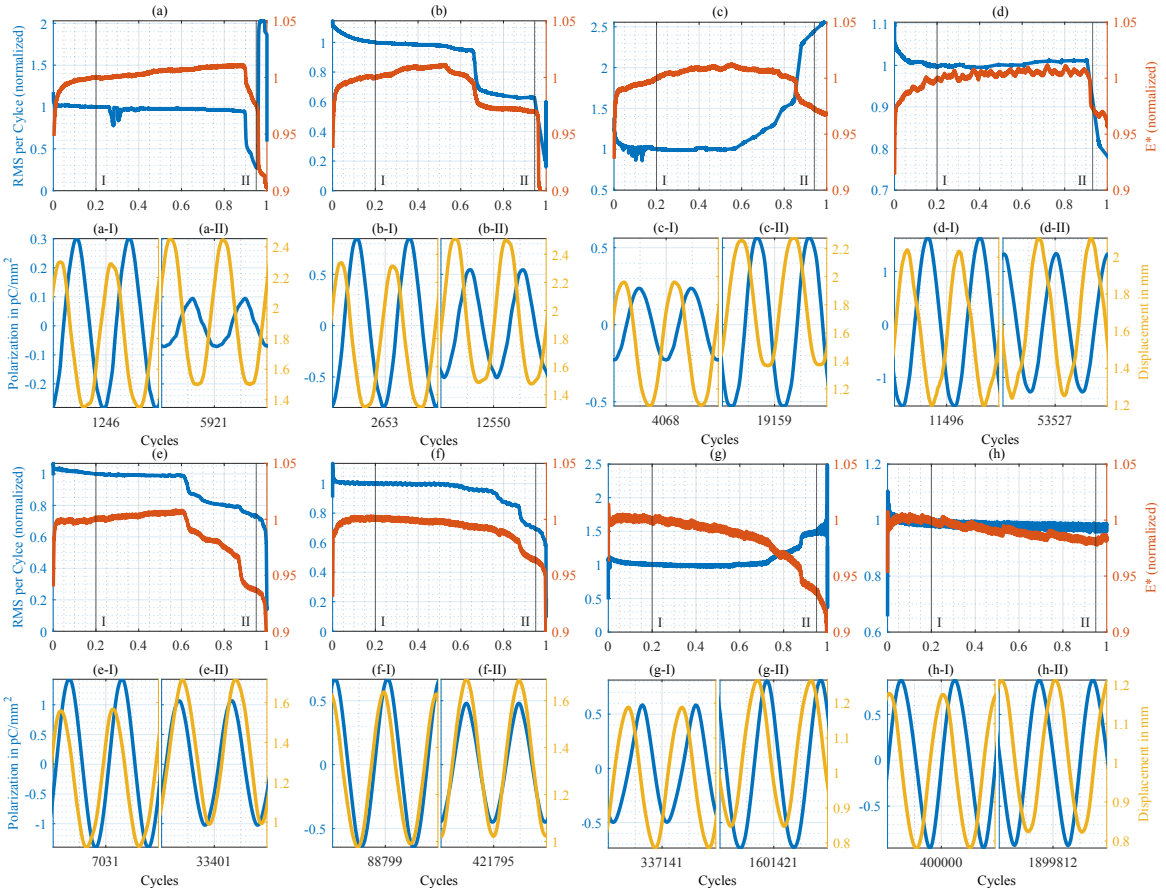

Figure 4. Normalized RMS polarization (left axis, blue line) and normalized dynamic modulus E^* (right axis, orange line) in relation to normalized cycles for 80% (a and b), 70% (c and d), 60% (e and f), and 50% (g and h) UTS. Markings I and II represent points of interest at 0.2 and 0.95 normalized service life, and a-h I and II the respective polarization and displacement data.

In the following sections, the behavior of all selected tested samples will be examined in more detail. Since the change in amplitude has proven to be the main indicator of a change in the composite, the RMS polarization will also be used here as a key figure. Figure 5 illustrates the results of all 48 tests conducted. The mechanical and electrical key figures presented were all recorded at 0.2 normalized cycles. In Figure 5a, the dynamic modulus is plotted in relation to the load levels. A one-way ANOVA ($\alpha = 0.05$) indicated that there is no significant change in the dynamic modulus at load levels of 50% and 60% of the UTS. However, a significant decline was observed at 70% and 80% of the UTS relative to 50% and 60%. As verified in Figure 5b, the different excitation frequencies at load levels of 50% (20 Hz) and 60% (10 Hz) UTS do not significantly influence the dynamic modulus. The higher load levels (70% and 80% UTS) were tested at a consistent frequency of 5 Hz, which shows a significant change in dynamic modulus, relative to 50% and 60%.

Furthermore, it is necessary to investigate whether the RMS polarization is influenced by the frequency and load level used. Figure 5c illustrates the RMS polarization in relation to varying load levels. Overall, there is a slight increase in RMS polarization as the load level rises. At the higher load levels (70% and 80%), measured at an excitation frequency of 5 Hz (as shown in Figure 5d), the median RMS polarization increases with load level; however, none of these changes are statistically significant according to one-way ANOVA ($\alpha = 0.05$). Meanwhile, Figure 5d presents the RMS polarization in relation to the excitation frequency, revealing a decrease in the median as frequency increases, which is also not significant according to one-way ANOVA. Consequently, no significant influences of frequency or load level on the RMS polarization can be observed.

Finally, the changes in polarization and stiffness will be compared. To achieve this, the mechanical and electrical key figures at 0.2 and 0.95 normalized cycles were taken (dynamic modulus and RMS

 doi:10.20944/preprints202506.2154.v1

polarization) and the absolute percentage change for each was calculated. The advantage of using absolute percentage change is that it does not depend on whether the polarization is increasing or decreasing, and the varying absolute values do not affect the resulting key figure. From a sensory perspective, the ratio of the absolute change in polarization to the absolute change in dynamic modulus reflects the sensitivity of the method, as shown in Figure 5e. A trend is apparent: greater changes in stiffness are associated with larger changes in polarization, showing a statistically significant positive relationship ($p < 0.001$, $R^2 = 0.434$). The samples exhibiting the least sensitivity—meaning they showed minimal changes in polarization despite significant changes in stiffness—were subjected to a load level of 50%. These samples had reached the maximum cycle count of 2 million, and testing was terminated before breakage occurred. Overall, changes in stiffness always result in a greater change in polarization. This study also reveals a high level of variance, which is also evident in the polarization results (see Figure 5c-d). Nevertheless, a correlation between the two examined key figures can be observed. The calculated sensitivity corresponds to 4.7 (% polarization per % dynamic modulus).

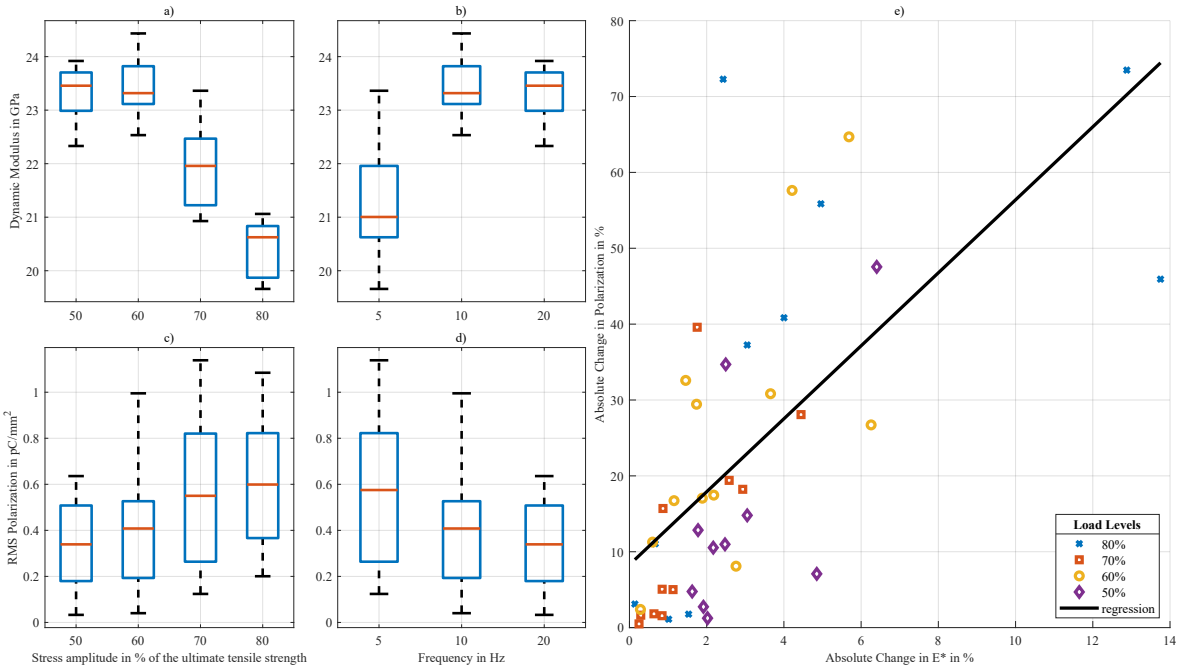

Figure 5. Representation of the mechanical and electrical variables of all samples. a) Dynamic modulus in relation to the load level in % at 0.2 normalized cycles. b) Dynamic modulus in relation to the frequency in Hz at 0.2 normalized cycles. c) Effective (root mean square) polarization in pC/mm^2 in relation to the load level in % at 0.2 normalized cycles. d) Effective (root mean square) polarization in pC/mm^2 in relation to the frequency in Hz at 0.2 normalized cycles. e) Absolute percentage change in polarization from 0.2 to 0.95 normalized cycles in relation to the absolute change in dynamic modulus in %. Blue represents the measurement points, and the black line represents the linear regression.

In summary, the change in RMS polarization serves as an indicator of changes in the dynamic modulus, which in turn reflect changes in stiffness. Both increases and decreases in polarization can be detected. Additionally, a minimum change of approximately 2% in dynamic modulus is necessary for this to affect the polarization significantly.

3.3. Cause of the Electrical Effect

When the authors first discovered the mechanoelectrical effect, several potential origins were considered [8], including the triboelectric effect, electrostriction, piezoelectricity, and the flexoelectric effect. The following discussion assesses whether these mechanisms could account for the measured signals.

In the author's previous investigation, a copper conductor was integrated into the composite [8]. In contrast, now a contactless setup was choosen, which by design cannot facilitate macroscopic

 doi:10.20944/preprints202506.2154.v1

contact–separation events, as required for effective charge seperation in Triboelectric Nanogenerators [73,74] or as observed in Cable Microphonics [54,75]. Although the absence of a directly attached electrode removes classical charge separation mechanisms, one might consider polarization effects arising from internal friction, such as the interaction between flax fibers and an epoxy matrix. However, relative motion is highly constrained as the flax fibers become embedded in and absorb the resin [76,77], making frictional charge transfer unlikely.

Electrostriction occurs in all insulators [78], but inverse electrostriction (the conversion of mechanical energy to electrical energy) requires an electrical bias [79]. Since this bias is absent in our case, this effect was ruled out.

The flexoelectric effect can occur in any crystal symmetry [80], but it requires a strain gradient that disrupts local centrosymmetry [81]. This phenomenon typically manifests during bending and is measured using a bending setup [82,83] Although flexoelectricity can also be observed under axial loading, it necessitates a gradient in mechanical properties, such as stiffness or thickness, along the specimen (cf. [84] and Appendix B). In natural fibers like flax, inherent structural heterogeneities often cause variations in both stiffness [85,86] and thickness [87], making them promising candidates for observing axial flexoelectric effects. Additionally, manufacturing imperfections—such as skewing—can further alter local stiffness, thus enhancing the flexoelectric response. Flexoelectricity has also been demonstrated in cellulose [82]—the fundamental building block of plant fibers [88] and therefore our composite, particularly in thin films, but its magnitude decreases significantly as the thickness increases [89]. Furthermore, the flexoelectric coefficient is several orders of magnitude smaller than the piezoelectric coefficient [90]. Thus, while the flexoelectric effect cannot be dismissed entirely, it is unlikely to be the primary factor behind our observations.

The piezoelectric effect, which requires a non-centrosymmetric crystal structure [80,91], has been observed in cellulose. In cellulose, hydroxyl groups are arranged non-centrosymmetrically through hydrogen bonding, leading to the formation of a dipole moment [92–95]. Both the direct [96] and converse [97] piezoelectric effects have been demonstrated in bulk materials (solid wood). The strength of the piezoelectric effects can vary significantly depending on the fiber direction [97] and pretreatment [92,98], which may explain the fluctuating material properties observed. Another indication of polarizability is the decrease in ε' with increasing frequency (as seen in [64] and in Appendix A), a phenomenon characteristic of orientation polarization, as seen in dipolar molecular chains [82,99]. Furthermore, Knuffel et al. found a correlation between the piezoelectric effect and stiffness in solid wood, a relationship also reflected in our results [100]. Furthermore, the piezoelectric effect depends on the mechanical amplitude [101], which is also the case in our experiments. Therefore, the piezoelectric effect can be identified as a potential cause of our observations.

3.4. Future Challenges

In this study, a mechanoelectric effect was observed in 48 samples, showing its potential for use in structural health monitoring under laboratory conditions. However, several challenges need to be addressed to make this suited for real-life conditions, which will be briefly discussed in this section.

First, the measurement setup presents a challenge. Conductive structures, such as foils and conductors, must be brought into proximity to the composite material, as contactless measurement is not always feasible. The introduction of these conductive structures may also influence the observed effect. Another challenge lies in the measurements themselves. The observed effects were relatively small and could be disturbed or obscured by electromagnetic coupling (EMC noise). A well-defined approach is necessary to ensure electromagnetic compatibility during measurements. Although a correlation between the measured signals and the stiffness was found, a problem could occur if the stiffness changes only slightly. This limitation could impact the effectiveness of our concept. Finally, the variability of the actual measurement signals should be addressed. However, it is possible that this measurement method only allows for relative monitoring due to fluctuations in signal strength. Further research is required to improve our understanding of the effect and enhance the overall consistency of the signals obtained. One possible explanation for the observed phenomena is the direction in

 doi:10.20944/preprints202506.2154.v1

which the fibers grew. A controlled orientation of these fibers could potentially lead to more consistent results.

Overall, the method described here offers a significant advantage and represents an initial step toward developing a new type of structural health monitoring system for natural fiber-reinforced polymers. Since this approach does not require the integration of sensors, it does not alter the mechanical properties of the composite material. Furthermore, a correlation exists between changes in stiffness and changes in polarization, establishing a direct connection between mechanical and electrical parameters. This feature provides a noteworthy advantage over other structural health monitoring systems and could provide an even greater advantage when used in combination with other structural health monitoring systems.

4. Conclusions

In this study, a mechanoelectric effect, likely of piezoelectric nature, was investigated in natural fiber-reinforced polymer for the first time across four different load levels using contactless measurements during dynamic mechanical analysis. The results show that the measured polarization is not statistically significant in relation to load levels and correlates with the dynamic modulus. Ultimately, monitoring changes in the electrical signal allows for predicting upcoming failures of nearly all the samples. Overall, the method described here offers a significant advantage and marks an important step toward the development of a new class of structural health monitoring systems for natural fiber-reinforced polymers. Unlike conventional approaches, it does not require embedded sensors, thereby preserving the composite material's mechanical properties. A clear correlation between changes in stiffness and polarization establishes a direct link between mechanical and electrical behavior. This feature provides a distinct advantage over existing systems and holds even greater potential when integrated with other structural health monitoring methods.

Author Contributions: Conceptualization, C. M.; methodology, C.M. and P. H.; software, C. M.; validation, C. M. and P. H.; formal analysis, C. M.; resources, A. W. and K. K.; writing—original draft preparation, C. M. and P. H.; writing—review and editing, A. W., K. K. and G. F.; visualization, C. M.; supervision, G. F.; project management, K. K.; funding acquisition, A. W. and K. K. All authors have read and agreed to the published version of the manuscript.

Funding: This work was supported by the Carl Zeiss Foundation through the project "Intelligent Composite Materials."

Data Availability Statement: Please contact the corresponding author.

Conflicts of Interest: Klaus-Peter Koch and Christoph Maier are named inventors on patent application US 20240035921, which is related to determining the condition of composite components and may be relevant to the subject matter of this work. The authors declare no other conflicts of interest.

Appendix A. Measurement of the Permittivity of Natural Fiber-Reinforced Polymers at Low Frequencies

A parallel-plate capacitor was manufactured following DIN 62631 from steel (1.4313) to test permittivity [102]. The measuring electrode has a diameter of 90 mm and is surrounded by a guard electrode with a width of 5 mm. There is a gap of approximately 0.5 mm between the measuring and guard electrodes. The counter electrode has a diameter of 100 mm. All plates were polished to achieve minimal roughness. The impedance analysis method was employed to measure the permittivity. A function generator (Hameg HMF 2550) was used to generate the sinusoidal voltage signal at the counter electrode and was captured using a measuring card (NI 9234), while current measurements were taken with an ammeter (Keysight B2987B) at the measuring electrode. Care was taken to keep the length of the measuring cables as short as possible. The function generator and ammeter were synchronized through the measurement card using the trigger output signal from the ammeter. The data from the ammeter and the measuring card are transferred to the PC via a USB connection. A

 doi:10.20944/preprints202506.2154.v1

manual open and short calibration was carried out before the measurement. The open-circuit reactance of the plate capacitor was first recorded in the open state, and then the contact resistance was measured in the short-circuit state. These reference measurements are used to compensate for systematic errors in the measurement setup. All measurements were conducted in an air-conditioned environment within a climate chamber (Binder MK112), which remained closed throughout the entire test duration. The measuring arrangement was successfully tested using polytetrafluoroethylene (PTFE), where ε' is supposed to be 2.1 [103,104]. Subsequently, measurements could be carried out with the natural fiber-reinforced polymer, which was produced using the same manufacturing process (compression molding) and pressing pressure (13.6 bar) as the rest of the study.

The relevant temperatures were determined in preliminary tests, and corresponded to 20°C, 30°C, and 40°C, at frequencies of 1 Hz, 2 Hz, 5 Hz, 10 Hz, 20 Hz, and 40 Hz. Five measurements were carried out for each frequency at each temperature. The amplitude and phase shift were determined for both the input voltage and the output current. The impedance Z then corresponds to

$$Z = \frac{|U|}{|I|} e^{j(\varphi_V - \varphi_I)} \tag{A1}$$

Z corresponds to the impedance, $|U|$ to the voltage amplitude, $|I|$ to the current amplitude, φ_V denotes the phase shift of the voltage wave, and φ_I indicates the phase shift of the current wave. The difference between the phases of the two oscillations results in the phase shift.

$$\theta = \varphi_V - \varphi_I \tag{A2}$$

where θ represents the phase shift between voltage and current; φ_V denotes the phase shift of the voltage wave, and φ_I indicates the phase shift of the current wave, both compared to a sine wave with a phase shift of 0. The resistance R and the reactance X can then be determined using impedance Z and the phase angle between voltage and current θ

$$R = Zcos(\theta) \tag{A3}$$

$$X = Zsin(\theta) \tag{A4}$$

where R corresponds to the resistance, X to the reactance, Z to the impedance and θ to the phase angle between voltage and current. The real and imaginary part of the permittivity can then be calculated.

$$\varepsilon' = \frac{-X}{\omega C_0 (X^2 + R^2)} \tag{A5}$$

$$\varepsilon'' = \frac{R}{\omega C_0 (X^2 + R^2)} \tag{A6}$$

In this context, ε' denotes the real part of permittivity, while ε'' represents the imaginary part of permittivity. The symbol R corresponds to resistance, and X stands for reactance. The term ω refers to the angular frequency, expressed as $2\pi f$, where f is the excitation frequency. Additionally, C_0 represents the capacitance in a vacuum.

$$C_0 = \frac{\varepsilon_0 A}{d} \tag{A7}$$

In this context, ε_0 represents the permittivity of free space, A denotes the area of the measuring electrode, and d indicates the separation between the capacitor plates.

The data presented in Figure A1 illustrate the frequency- and temperature-dependent complex permittivity of a natural fiber-reinforced polymer, measured using a plate capacitor. The error bars in both diagrams represent five independent measurements for each data point and reflect the associated measurement variance.

 doi:10.20944/preprints202506.2154.v1

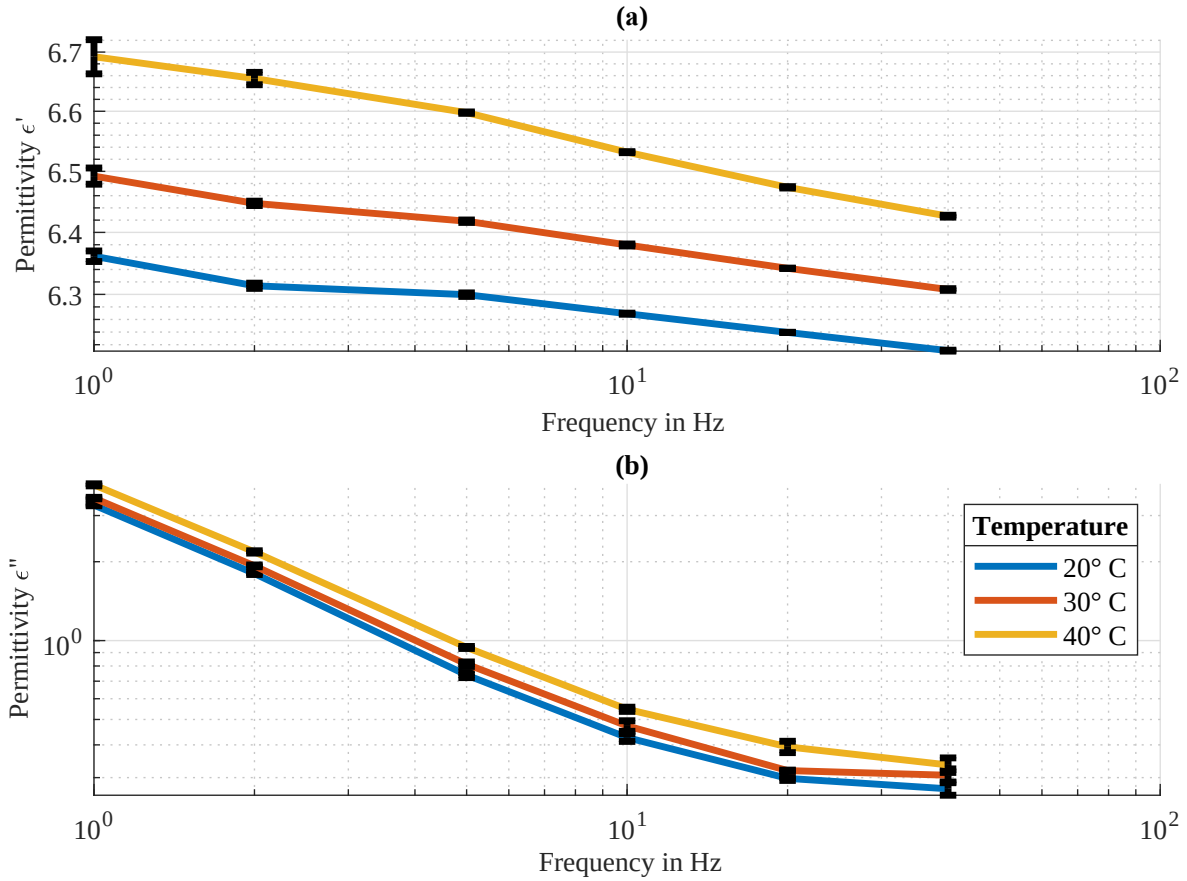

Figure A1. Real and imaginary part of the permittivity for frequencies of 1 Hz, 2 Hz, 5 Hz, 10 Hz, 20 Hz and 40 Hz in logarithmic scale for temperatures of 20°C (blue), 30°C (red) and 40°C (yellow). (a) Real part of the permittivity ε' in linear scale. (b) Imaginary part of the permittivity ε'' in logarithmic scale.

Figure A1a shows the real part of the permittivity (ε') over a frequency range of 1 Hz to 40 Hz at three temperatures: 20°C, 30°C, and 40°C. As the frequency increases, ε' decreases. Generally, higher temperatures result in higher permittivity values. At low frequencies and lower temperatures, the increase in ε' is mainly due to the polarization of water dipoles in the pectocellulosic fibers [61,105]. These dipoles come from water molecules absorbed by the fibers and form a thin molecular layer, contributing to the material's ability to store electrical energy [105].

Figure A1b shows the imaginary part of the permittivity (ε'') in the same frequency range. The almost linear decline of ε'' on a double-logarithmic scale at frequencies between 1-10 Hz indicates losses due to a constant conductivity comparable to a fixed electrical resistance. This behavior is commonly referred to as the DC conductivity effect [61]. Additionally, ε'' increases with rising temperatures, consistent with thermally activated charge transport [106].

The required values for ε' and ε'' can be found in Table A1.

Table A1. ε' and ε'' used for further calculation at different excitation frequencies.

UTS in %	Excitation Frequency (Hz)	Temperature (°C)	ε'	ε''
80	5	40	6.6	0.94
70	5	40	6.6	0.94
60	10	40	6.53	0.55
50	20	40	6.47	0.39

Appendix B. Simulation of Mechanoelectrical Effects with Variable Stiffness

The following section presents a simulation using bar elements to demonstrate how different stiffness characteristics along a sample influence the measured signal. The goal of this simulation is

 doi:10.20944/preprints202506.2154.v1

not to replicate the exact effects or materials described in previous research but rather to illustrate the concepts related to the transition from mechanical to electrical variables. To achieve this, some simplifications have been made.

First, we assume that the material behaves in a purely linear-elastic manner. The cross-sectional area is considered constant at (3.74 mm^2, with a width of 17 mm and a depth of 2.2 mm), and the initial length of each element is fixed at 1 mm over a total sample length of 100 mm. One end of the specimen is firmly clamped, while a force is applied at the other. As in the experimental setup, the load is applied in a tension-tension configuration with a frequency of 5 Hz, a mean force of 11 kN, and an amplitude of 10 kN.

Three cases are investigated, each varying in stiffness (cf. Figure A2a-c). All cases exhibit a sinusoidal variation around a central value of 30 GPa with an amplitude of 0.3 GPa along the sample length. Upon applying the force, the inverse stiffness matrix is used to calculate the nodal displacement, from which the strain is then obtained. Both piezoelectric and flexoelectric effects are included in the simulation, with the corresponding coefficients set to 1.

The following applies to the piezoelectric effect [101]:

$$P_k = e_{kij}\epsilon_{ij} \tag{A8}$$

Here P_k denotes the electrical polarization, e_{kij} the piezoelectric coefficient of the third-rank tensor, and $\epsilon_{i,j}$ the strain tensor. In this case, the polarization is considered in the transverse direction ($k = 3$), with strain in the longitudinal direction ($i = 1$, $j = 1$). The result is

$$P_3 = e_{311}\epsilon_{11} \tag{A9}$$

Here, P_3 corresponds to the polarization perpendicular to the load direction, e_{311} to the corresponding piezoelectric constant, and ϵ_{11} to the strain in the longitudinal direction.

The following applies to the flexoelectric effect [81]:

$$P_k = \mu_{klij}\frac{\partial \epsilon_{ij}}{\partial x_l} \tag{A10}$$

Here P_k denotes the electrical polarization, μ_{klij} the flexoelectric coefficient as a fourth-rank tensor, and $\frac{\partial \epsilon_{ij}}{\partial x_l}$ the gradient of the strain tensor. In this case, the polarization in the transverse direction ($k = 3$) is also considered, with longitudinal strain ($i = 1$, $j = 1$), whose spatial gradient occurs along the bar axis ($l = 1$). From this follows:

$$P_3 = \mu_{3111}\frac{\partial \epsilon_{11}}{\partial x_1} \tag{A11}$$

Here P_3 describes the polarization perpendicular to the load direction, μ_{3111} the corresponding flexoelectric coefficient, and $\frac{\partial \epsilon_{11}}{\partial x_1}$ the strain gradient along the load direction.

It is assumed that the entire lateral surface is, in both cases, electrically connected. The total charge is obtained by summing the polarization times the effective lateral area of each element. Figure A2d-f illustrates the resulting strain during the first time step for the respective stiffness characteristics presented in Figure A2a-c, with an applied force of 11 kN. Elements with lower stiffness experience greater strains, while those with higher stiffness yield lower strains. Figure A2g-i shows the strain gradient (also for cases a-c), which is particularly important for considering the flexoelectric effect. At this stage, all mechanical quantities have been determined for the first time step. This procedure can then be repeated for all subsequent time steps.

 doi:10.20944/preprints202506.2154.v1

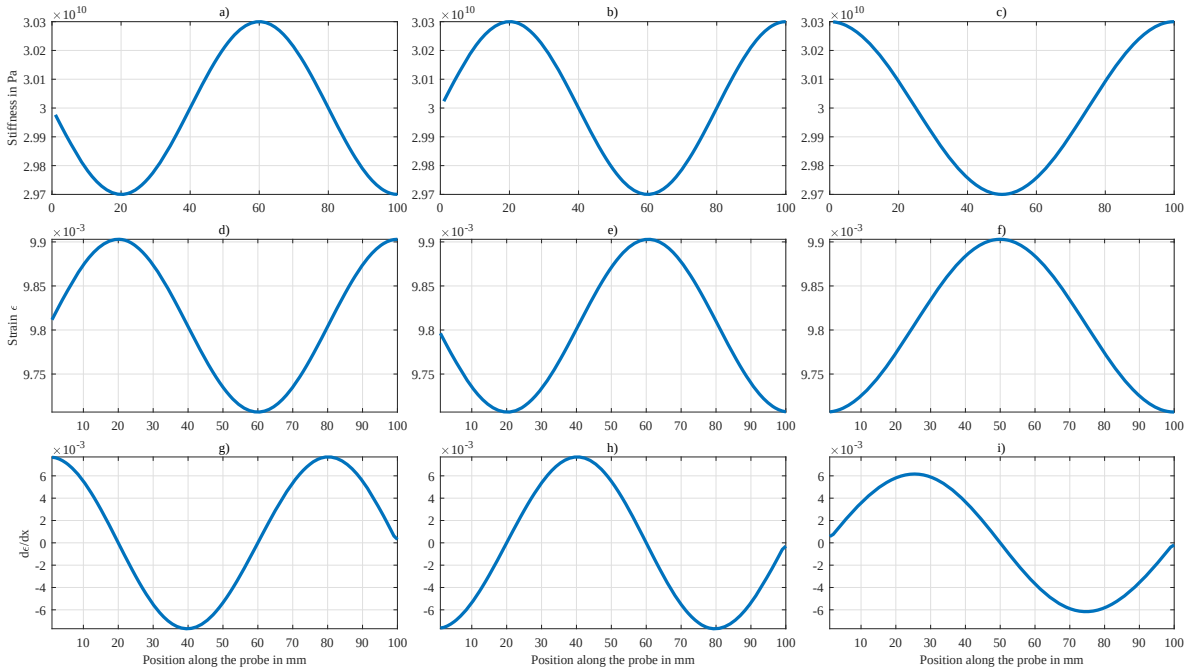

Figure A2. a-c) Representation of the three stiffness characteristics along the probe. d-f) Resulting strain along the probe for the cases from a-c, respectively. g-i) Derivation of the strain along the probe for the cases from a-c, respectively.

Figure A3a-c displays the total change in length of the sample under sinusoidal loading, corresponding to the stiffness characteristics from Figure A2a-c, respectively. Figure A3d-f illustrates the charge displaced by the piezoelectric effect over time, corresponding to the stiffness characteristics of Figure A2a-c. It can be observed that approximately the same amount of charge is displaced in all three cases, and this displacement is always in phase with the total change in length of the sample.

Figure A3g-i presents the charge over time due to the flexoelectric effect, again related to the respective stiffness curves from Figure A2a-c. In Figure A3g, the resulting charge is in phase with the total change in length, with all charges being positive, while in Figure A3h, it is out of phase by 180, with all charges being negative. Conversely, no charge displacement is in Figure A3i.

The differences in phase behavior are attributed to the respective stiffness characteristics of the materials. Since the entire surface is contacted and the flexoelectric coefficient was set to 1, the effective charge arises from the sum of the strain gradients (and the lateral surface) shown in Figure A2g-i. In cases g and h, the contributions over the first wavelength cancel each other out. Only the final quarter of the wavelength contributes to the flexoelectric effect, as it cannot be compensated. In Figure A3g, the resulting charge is positive, indicating that it is in phase with the total change in length. In Figure A3h, the negative sign leads to a phase shift. In Figure A3i, all strain gradients cancel each other out completely, resulting in no charge displacement.

To summarize, the charge displacement induced by the piezoelectric effect corresponds to the total change in length in all cases. In contrast, the flexoelectric effect requires a spatial variation in stiffness that does not cancel out over the entire material. If there is a change in stiffness, the resulting signal can either be in phase or 180° out of phase with the total relative displacement of the sample. Additionally, a variation in cross-sectional area, such as a slope in the material, can contribute to a corresponding effect.

 doi:10.20944/preprints202506.2154.v1

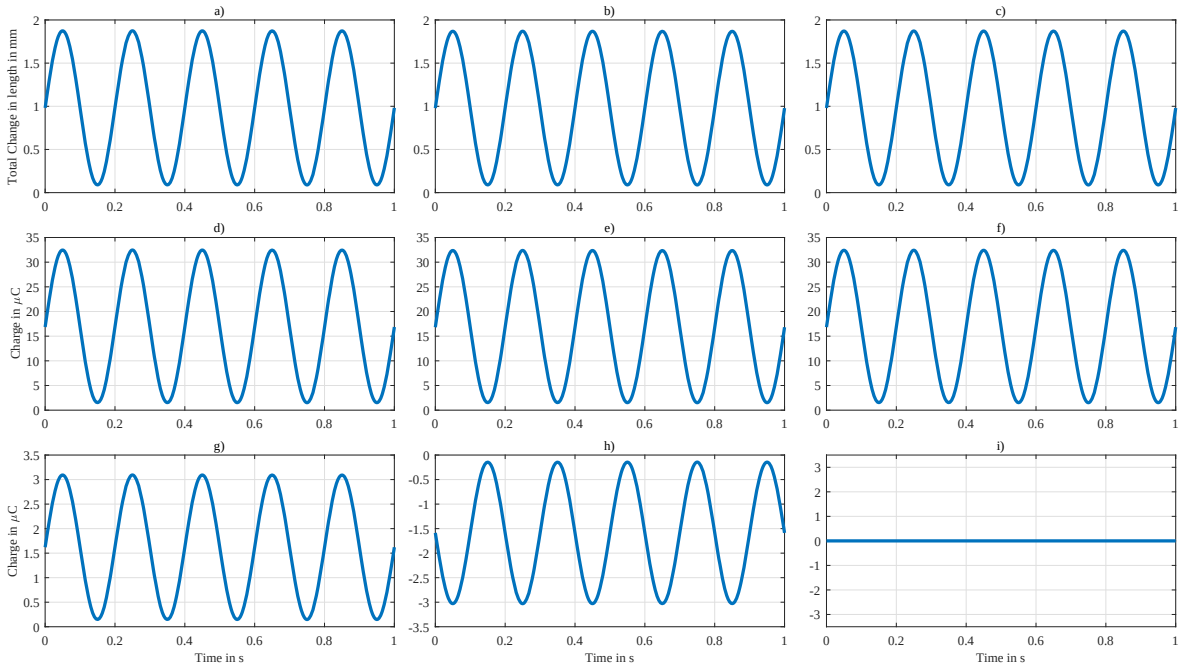

Figure A3. a-c) Total relative displacement over time for the three different characteristics from Figure A2a-c, respectively. d-f) Piezoelectric effect over time for the three different characteristics from Figure A2a-c, respectively. g-i) Flexoelectric effect over time for the three different characteristics from Figure A2a-c, respectively.

Appendix C. Values Used for Normalization

Table A2. Values used for normalization

Specimen	E* in MPa	RMS Polarization	Cycles
P04 P1	20.644,69	0,2073	6.233
P04 P2	21.061,19	0,5786	13.268
P06 P1	20.927,75	0,1669	20.344
P07 P5	21.819,09	1,1318	57.482
P09 P4	23.372,05	0,9952	35.159
P09 P5	23.903,58	0,4608	443.995
P10 P6	22.948,86	0,3654	1.685.707
P11 P3	23.072,00	0,6357	2.000.000

References

1. Niels de Beus.; Michael Carus.; Martha Barth. Carbon Footprint and Sustainability of Different Natural Fibres for Biocomposites and Insulation Material: Study providing data for the automotive and insulation industry.
2. Summerscales, J.; Dissanayake, N.P.; Virk, A.S.; Hall, W. A review of bast fibres and their composites. Part 1 – Fibres as reinforcements. *Composites Part A: Applied Science and Manufacturing* **2010**, *41*, 1329–1335. https://doi.org/10.1016/j.compositesa.2010.06.001.
3. Wambua, P.; Ivens, J.; Verpoest, I. Natural fibres: can they replace glass in fibre reinforced plastics? *Composites Science and Technology* **2003**, *63*, 1259–1264. https://doi.org/10.1016/S0266-3538(03)00096-4.
4. Joshi, S.; Drzal, L.; Mohanty, A.; Arora, S. Are natural fiber composites environmentally superior to glass fiber reinforced composites? *Composites Part A: Applied Science and Manufacturing* **2004**, *35*, 371–376. https://doi.org/10.1016/j.compositesa.2003.09.016.
5. ANDERSONS, J.; SPARNINS, E.; JOFFE, R.; WALLSTROM, L. Strength distribution of elementary flax fibres. *Composites Science and Technology* **2005**, *65*, 693–702. https://doi.org/10.1016/j.compscitech.2004.10.001.
6. Ren, B.; Mizue, T.; Goda, K.; Noda, J. Effects of fluctuation of fibre orientation on tensile properties of flax sliver-reinforced green composites. *Composite Structures* **2012**, *94*, 3457–3464. https://doi.org/10.1016/j.compstruct.2012.06.002.

 doi:10.20944/preprints202506.2154.v1

7. Farrar, C.R.; Worden, K. An introduction to structural health monitoring. *Philosophical transactions. Series A, Mathematical, physical, and engineering sciences* **2007**, *365*, 303–315. https://doi.org/10.1098/rsta.2006.1928.
8. Maier, C.; Koch, K.P.; Fischer, G. Measuring Deformation in Natural Fiber-Reinforced Polymer Using Mechanoelectrical Effect. *IEEE Sensors Letters* **2024**, *8*, 1–4. https://doi.org/10.1109/LSENS.2024.3427376.
9. Hassani, S.; Mousavi, M.; Gandomi, A.H. Structural Health Monitoring in Composite Structures: A Comprehensive Review. *Sensors (Basel, Switzerland)* **2021**, *22*. https://doi.org/10.3390/s22010153.
10. Baron, P.; Lenz, P.; Wittmann, A.; Fischer, G. Integrity-Sensing Based on Surface Roughness of Copper Conductors for Future Use in Natural Fiber Composites. *IEEE Sensors Letters* **2021**, *5*, 1–4. https://doi.org/10.1109/LSENS.2021.3061143.
11. Baron, P. *Entwicklung eines mechano-elektrischen Sensorelements zur strukturellen Bauteilüberwachung von Naturfaserverbundwerkstoffen mittels hochfrequenter Wechselströme*; Vol. 46, *FAU Forschungen Reihe B*, FAU University Press: Erlangen, 2024.
12. Wen, J.; Xia, Z.; Choy, F. Damage detection of carbon fiber reinforced polymer composites via electrical resistance measurement. *Composites Part B: Engineering* **2011**, *42*, 77–86. https://doi.org/10.1016/j.compositesb.2010.08.005.
13. Brown, S.C.; Robert, C.; Koutsos, V.; Ray, D. Methods of modifying through-thickness electrical conductivity of CFRP for use in structural health monitoring, and its effect on mechanical properties – A review. *Composites Part A: Applied Science and Manufacturing* **2020**, *133*, 105885. https://doi.org/10.1016/j.compositesa.2020.105885.
14. Burkov, M.; Eremin, A. Hybrid CFRP/SWCNT Composites with Enhanced Electrical Conductivity and Mechanical Properties. *Journal of Materials Engineering and Performance* **2018**, *27*, 5984–5991. https://doi.org/10.1007/s11665-018-3695-x.
15. Du, J.; Zeng, J.; Wang, H.; Ding, H.; Wang, H.; Bi, Y. Using acoustic emission technique for structural health monitoring of laminate composite: A novel CNN-LSTM framework. *Engineering Fracture Mechanics* **2024**, *309*, 110447. https://doi.org/10.1016/j.engfracmech.2024.110447.
16. Ghadarah, N.; Ayre, D. A Review on Acoustic Emission Testing for Structural Health Monitoring of Polymer-Based Composites. *Sensors (Basel, Switzerland)* **2023**, *23*. https://doi.org/10.3390/s23156945.
17. Masmoudi, S.; El Mahi, A.; Turki, S. Fatigue behaviour and structural health monitoring by acoustic emission of E-glass/epoxy laminates with piezoelectric implant. *Applied Acoustics* **2016**, *108*, 50–58. https://doi.org/10.1016/j.apacoust.2015.10.024.
18. Ghezzo, F.; Huang, Y.; Nemat-Nasser, S. Onset of Resin Micro-Cracks in Unidirectional Glass Fiber Laminates with Integrated SHM Sensors: Experimental Results. *Structural Health Monitoring* **2009**, *8*, 477–491. https://doi.org/10.1177/1475921709340976.
19. Tuloup, C.; Harizi, W.; Aboura, Z.; Meyer, Y. Integration of piezoelectric transducers (PZT and PVDF) within polymer-matrix composites for structural health monitoring applications: new success and challenges. *International Journal of Smart and Nano Materials* **2020**, *11*, 343–369. https://doi.org/10.1080/19475411.2020.1830196.
20. Niezrecki, C.; Baqersad, J.; Sabato, A. Digital Image Correlation Techniques for NDE and SHM. *Mechanical Engineering Publications* **2018**, *111*, 1–46. https://doi.org/10.1007/978-3-319-30050-4{_}47-1.
21. Yu, B.; Blanc, R.; Soutis, C.; Withers, P.J. Evolution of damage during the fatigue of 3D woven glass-fibre reinforced composites subjected to tension–tension loading observed by time-lapse X-ray tomography. *Composites Part A: Applied Science and Manufacturing* **2016**, *82*, 279–290. https://doi.org/10.1016/j.compositesa.2015.09.001.
22. Hung, Y.Y.; Yang, L.X.; Huang, Y.H., Eds. *Non-destructive evaluation (NDE) of composites: digital shearography*; Elsevier, 2013. https://doi.org/10.1533/9780857093554.1.84.
23. Ye, X.W.; Dong, C.Z.; Liu, T. A Review of Machine Vision-Based Structural Health Monitoring: Methodologies and Applications. *Journal of Sensors* **2016**, *2016*, 1–10. https://doi.org/10.1155/2016/7103039.
24. Payawal, J.M.G.; Kim, D.K. Image-Based Structural Health Monitoring: A Systematic Review. *Applied Sciences* **2023**, *13*, 968. https://doi.org/10.3390/app13020968.
25. Shah, D.U. Developing plant fibre composites for structural applications by optimising composite parameters: a critical review. *Journal of Materials Science* **2013**, *48*, 6083–6107. https://doi.org/10.1007/s10853-013-7458-7.
26. Lotfi, A.; Li, H.; Dao, D.V.; Prusty, G. Natural fiber–reinforced composites: A review on material, manufacturing, and machinability. *Journal of Thermoplastic Composite Materials* **2021**, *34*, 238–284. https://doi.org/10.1177/0892705719844546.
27. BComp Ltd. *ampliTex TM*, 2021.

 doi:10.20944/preprints202506.2154.v1

28. Rask, M.; Madsen, B. Twisting of fibres in yarns for natural fibre composites. 2011. 18th International Conference on Composite Materials, ICCM18 ; Conference date: 21-08-2011 Through 26-08-2011.
29. Baley, C.; Gomina, M.; Breard, J.; Bourmaud, A.; Drapier, S.; Ferreira, M.; Le Duigou, A.; Liotier, P.J.; Ouagne, P.; Soulat, D.; et al. Specific features of flax fibres used to manufacture composite materials. *International Journal of Material Forming* **2019**, *12*, 1023–1052. https://doi.org/10.1007/s12289-018-1455-y.
30. Entropy Resins. *305 - Compression Moulding Epoxy*, 2024.
31. Entropy Resins. *CPF Fast*, 2024.
32. Kern-sohn. *Kern Digitalscale EMB 1000-2*, 2024.
33. Muthuvel, B.; Bhattacharyya, D.; Bickerton, S. Development of innovative flow visualisation methods to investigate the stages of Wet Compression Moulding (WCM) process. *IOP Conference Series: Materials Science and Engineering* **2020**, *912*, 052013. https://doi.org/10.1088/1757-899X/912/5/052013.
34. DIN EN ISO 527-4: Plastics - Determination of tensile properties, Part 4: Test conditions for isotropic and orthotropic fibre-reinforced plastic composites, 2023-07-00.
35. BS ISO 13003: Fibre-reinforced plastics. Determination of fatigue properties under cyclic loading conditions , 2004-02-03.
36. ASTM D 3039: Standard Test Method for Tensile Properties of Polymer Matrix Composite Materials, 2017-00-00.
37. ASTM D 3479: Standard Test Method for Tension-Tension Fatigue of Polymer Matrix Composite Materials, 2019-00-00.
38. Roe, P.J.; Ansell, M.P. Jute-reinforced polyester composites. *Journal of Materials Science* **1985**, *20*, 4015–4020. https://doi.org/10.1007/BF00552393.
39. Wang, J.; Li, Y.; Yu, T.; Li, Q.; Li, Z. Anisotropic behaviors of moisture absorption and hygroscopic swelling of unidirectional flax fiber reinforced composites. *Composite Structures* **2022**, *297*, 115941. https://doi.org/10.1016/j.compstruct.2022.115941.
40. Liang, S.; Gning, P.B.; Guillaumat, L. A comparative study of fatigue behaviour of flax/epoxy and glass/epoxy composites. *Composites Science and Technology* **2012**, *72*, 535–543. https://doi.org/10.1016/j.compscitech.2012.01.011.
41. Jeannin, T.; Gabrion, X.; Ramasso, E.; Placet, V. About the fatigue endurance of unidirectional flax-epoxy composite laminates. *Composites Part B: Engineering* **2019**, *165*, 690–701. https://doi.org/10.1016/j.compositesb.2019.02.009.
42. El Sawi, I.; Fawaz, Z.; Zitoune, R.; Bougherara, H. An investigation of the damage mechanisms and fatigue life diagrams of flax fiber-reinforced polymer laminates. *Journal of Materials Science* **2014**, *49*, 2338–2346. https://doi.org/10.1007/s10853-013-7934-0.
43. Katunin, A.; Wachla, D.; Santos, P.; Reis, P.N. Fatigue life assessment of hybrid bio-composites based on self-heating temperature. *Composite Structures* **2023**, *304*, 116456. https://doi.org/10.1016/j.compstruct.2022.116456.
44. Jouenne, J.B.; Barbier, D.; Hounkpati, V.; Cauret, L.; Vivet, A. Influence of flax fibers on the curing kinetics of bio-based epoxy resin. *Journal of Materials Science* **2024**, *59*, 12418–12432. https://doi.org/10.1007/s10853-024-09891-z.
45. Vyazovkin, S. Isoconversional Kinetics of Polymers: The Decade Past. *Macromolecular rapid communications* **2017**, *38*. https://doi.org/10.1002/marc.201600615.
46. Mahboob, Z.; Bougherara, H. Fatigue of flax-epoxy and other plant fibre composites: Critical review and analysis. *Composites Part A: Applied Science and Manufacturing* **2018**, *109*, 440–462. https://doi.org/10.1016/j.compositesa.2018.03.034.
47. Jeannin, T.; Berges, M.; Gabrion, X.; Léger, R.; Person, V.; Corn, S.; Piezel, B.; Ienny, P.; Fontaine, S.; Placet, V. Influence of hydrothermal ageing on the fatigue behaviour of a unidirectional flax-epoxy laminate. *Composites Part B: Engineering* **2019**, *174*, 107056. https://doi.org/10.1016/j.compositesb.2019.107056.
48. Liang, S.; Gning, P.B.; Guillaumat, L. Properties evolution of flax/epoxy composites under fatigue loading. *International Journal of Fatigue* **2014**, *63*, 36–45. https://doi.org/10.1016/j.ijfatigue.2014.01.003.
49. Carvalho, G.B.; Canevarolo, S.; de Sousa, J.A. Correlation of fatigue behavior and dynamic mechanical properties of hybrid composites of polypropylene/short glass fibers/hollow glass beads. *Journal of Thermoplastic Composite Materials* **2023**, *36*, 2233–2259. https://doi.org/10.1177/0892705721993190.
50. El Archi, Y.; Lahellec, N.; Lejeunes, S.; Jouan, A.; Tranquart, B. Multiscale simulation and experimental analysis of damping in CFRP structures containing rubber. *Composite Structures* **2022**, *289*, 115456. https://doi.org/10.1016/j.compstruct.2022.115456.

 doi:10.20944/preprints202506.2154.v1

51. Saba, N.; Jawaid, M.; Alothman, O.Y.; Paridah, M.T. A review on dynamic mechanical properties of natural fibre reinforced polymer composites. *Construction and Building Materials* **2016**, *106*, 149–159. https://doi.org/10.1016/j.conbuildmat.2015.12.075.
52. Surya Nagendra, P.; Prasad, V.; Ramji, K. A Study on Dynamic Mechanical Analysis of Natural Nano Banana Particle Filled Polymer Matrix Composites. *Materials Today: Proceedings* **2017**, *4*, 9081–9086. https://doi.org/10.1016/j.matpr.2017.07.262.
53. Idicula, M.; Malhotra, S.K.; Joseph, K.; Thomas, S. Dynamic mechanical analysis of randomly oriented intimately mixed short banana/sisal hybrid fibre reinforced polyester composites. *Composites Science and Technology* **2005**, *65*, 1077–1087. https://doi.org/10.1016/j.compscitech.2004.10.023.
54. Kaiser, K.L.; Palmer, K.I. Cable transient voltages due to microphonics. *Journal of Electrostatics* **2007**, *65*, 723–727. https://doi.org/10.1016/j.elstat.2007.05.008.
55. Tian, D.; Jeong, D.Y.; Fu, Z.; Chu, B. Flexoelectric Effect of Ferroelectric Materials and Its Applications. *Actuators* **2023**, *12*, 114. https://doi.org/10.3390/act12030114.
56. Wang, H.; Adamski, N.; Mu, S.; van de Walle, C.G. Piezoelectric effect and polarization switching in Al1− x Sc x N. *Journal of Applied Physics* **2021**, *130*. https://doi.org/10.1063/5.0056485.
57. Zhang, H.X.; Wang, P.F.; Yao, C.G.; Chen, S.P.; Cai, K.D.; Shi, F.N. Recent advances of ferro-/piezoelectric polarization effect for dendrite-free metal anodes. *Rare Metals* **2023**, *42*, 2516–2544. https://doi.org/10.1007/s12598-023-02319-8.
58. Griffiths, D.J. *Introduction to Electrodynamics*, 1st ed. ed.; Cambridge University Press: Cambridge, 2017.
59. Kersani, M.; Lomov, S.V.; van Vuure, A.W.; Bouabdallah, A.; Verpoest, I. Damage in flax/epoxy quasi-unidirectional woven laminates under quasi-static tension. *Journal of Composite Materials* **2015**, *49*, 403–413. https://doi.org/10.1177/0021998313519282.
60. Saadati, Y.; Lebrun, G.; Chatelain, J.F.; Beauchamp, Y. Experimental investigation of failure mechanisms and evaluation of physical/mechanical properties of unidirectional flax–epoxy composites. *Journal of Composite Materials* **2020**, *54*, 2781–2801. https://doi.org/10.1177/0021998320902243.
61. Karray, M.; Triki, A.; Poilâne, C.; Picart, P.; Gargouri, M. Dielectric relaxation phenomena in flax fibers composite. *Fibers and Polymers* **2016**, *17*, 88–96. https://doi.org/10.1007/s12221-016-5552-6.
62. Triki, A.; Karray, M.; Poilâne, C.; Picart, P.; Gargouri, M. Dielectric analysis of the interfacial polarization of alkali treated woven flax fibers reinforced epoxy composites. *Journal of Electrostatics* **2015**, *76*, 67–72. https://doi.org/10.1016/j.elstat.2015.05.017.
63. Zhang, S.; Li, Y.; Zheng, Z. Effect of physiochemical structure on energy absorption properties of plant fibers reinforced composites: Dielectric, thermal insulation, and sound absorption properties. *Composites Communications* **2018**, *10*, 163–167. https://doi.org/10.1016/j.coco.2018.09.006.
64. Baron, P.; Lenz, P.; Koch, K.P.; Wittmann, A.; Fischer, G. Dielectric properties of unidirectional and biaxial flax/epoxy composites at frequencies up to 1 GHz. *Materials Today Communications* **2023**, *36*, 106656. https://doi.org/10.1016/j.mtcomm.2023.106656.
65. Ueki, Y.; Lilholt, H.; Madsen, B. Stiffening effect of fatigue and creep loading in unidirectional flax fibre/epoxy composites. *IOP Conference Series: Materials Science and Engineering* **2018**, *388*, 012018. https://doi.org/10.1088/1757-899X/388/1/012018.
66. Kek, T.; Potočnik, P.; Misson, M.; Bergant, Z.; Sorgente, M.; Govekar, E.; Šturm, R. Characterization of Biocomposites and Glass Fiber Epoxy Composites Based on Acoustic Emission Signals, Deep Feature Extraction, and Machine Learning. *Sensors (Basel, Switzerland)* **2022**, *22*. https://doi.org/10.3390/s22186886.
67. Haggui, M.; El Mahi, A.; Jendli, Z.; Akrout, A.; Haddar, M. Static and fatigue characterization of flax fiber reinforced thermoplastic composites by acoustic emission. *Applied Acoustics* **2019**, *147*, 100–110. https://doi.org/10.1016/j.apacoust.2018.03.011.
68. Yosuke Ueki.; Hans Lilholt.; Bo Madsen. Fatigue behaviour of uni-directional flax fibre/epoxy composites. *Proceedings of the 20th International Conference on Composite Materials* **2015**.
69. Asgarinia, S.; Viriyasuthee, C.; Phillips, S.; Dubé, M.; Baets, J.; van Vuure, A.; Verpoest, I.; Lessard, L. Tension–tension fatigue behaviour of woven flax/epoxy composites. *Journal of Reinforced Plastics and Composites* **2015**, *34*, 857–867. https://doi.org/10.1177/0731684415581527.
70. Shah, D.U. Damage in biocomposites: Stiffness evolution of aligned plant fibre composites during monotonic and cyclic fatigue loading. *Composites Part A: Applied Science and Manufacturing* **2016**, *83*, 160–168. https://doi.org/10.1016/j.compositesa.2015.09.008.

 doi:10.20944/preprints202506.2154.v1

71. Wielage, B.; Lampke, T.; Utschick, H.; Soergel, F. Processing of natural-fibre reinforced polymers and the resulting dynamic–mechanical properties. *Journal of Materials Processing Technology* **2003**, *139*, 140–146. https://doi.org/10.1016/S0924-0136(03)00195-X.
72. Shen, Y.; Tan, J.; Fernandes, L.; Qu, Z.; Li, Y. Dynamic Mechanical Analysis on Delaminated Flax Fiber Reinforced Composites. *Materials (Basel, Switzerland)* **2019**, *12*. https://doi.org/10.3390/ma12162559.
73. Bai, P.; Zhu, G.; Jing, Q.; Yang, J.; Chen, J.; Su, Y.; Ma, J.; Zhang, G.; Wang, Z.L. Membrane–Based Self–Powered Triboelectric Sensors for Pressure Change Detection and Its Uses in Security Surveillance and Healthcare Monitoring. *Advanced functional materials* **2014**, *24*, 5807–5813. https://doi.org/10.1002/adfm.201401267.
74. Zhang, H.; Quan, L.; Chen, J.; Xu, C.; Zhang, C.; Dong, S.; Lü, C.; Luo, J. A general optimization approach for contact-separation triboelectric nanogenerator. *Nano Energy* **2019**, *56*, 700–707. https://doi.org/10.1016/j.nanoen.2018.11.062.
75. Perls, T.A. Electrical Noise from Instrument Cables Subjected to Shock and Vibration. *Journal of Applied Physics* **1952**, *23*, 674–680. https://doi.org/10.1063/1.1702277.
76. Le Duigou, A.; Kervoelen, A.; Le Grand, A.; Nardin, M.; Baley, C. Interfacial properties of flax fibre–epoxy resin systems: Existence of a complex interphase. *Composites Science and Technology* **2014**, *100*, 152–157. https://doi.org/10.1016/j.compscitech.2014.06.009.
77. Maier, C.; Beckmann, A.; Wittmann, A.; Koch, K.P.; Fischer, G. Investigation of the Discrepancy Between Optically and Gravimetrically Calculated Fiber Volume Fraction in Flax-Fiber-Reinforced Polymer. *Journal of Composites Science* **2025**, *9*, 103. https://doi.org/10.3390/jcs9030103.
78. Sundar, V.; Newnham, R.E. Converse method measurements of electrostriction coefficients in low-K dielectrics. *Materials Research Bulletin* **1996**, *31*, 545–554. https://doi.org/10.1016/s0025-5408(96)00035-9.
79. Yu, J.; Janolin, P.E. Defining "giant" electrostriction. *Journal of Applied Physics* **2022**, *131*. https://doi.org/10.1063/5.0079510.
80. Tagantsev, A.K.; Yudin, P.V. Flexoelectricity in Solids **2016**. https://doi.org/10.1142/9764.
81. Jianfeng Lu.; Xu Liang.; Shuling Hu. Flexoelectricity in Solid Dielectrics: From Theory to Applications. *Computers, Materials & Continua* **2015**, *45*, 145–162. https://doi.org/10.3970/cmc.2015.045.145.
82. Trellu, H.; Le Scornec, J.; Leray, N.; Moreau, C.; Villares, A.; Cathala, B.; Guiffard, B. Flexoelectric and piezoelectric effects in micro- and nanocellulose films. *Carbohydrate polymers* **2023**, *321*, 121305. https://doi.org/10.1016/j.carbpol.2023.121305.
83. Zubko, P.; Catalan, G.; Buckley, A.; Welche, P.R.L.; Scott, J.F. Strain-gradient-induced polarization in SrTiO3 single crystals. *Physical review letters* **2007**, *99*, 167601. https://doi.org/10.1103/PhysRevLett.99.167601.
84. Jiang, X.; Huang, W.; Zhang, S. Flexoelectric nano-generator: Materials, structures and devices. *Nano Energy* **2013**, *2*, 1079–1092. https://doi.org/10.1016/j.nanoen.2013.09.001.
85. Lefeuvre, A.; Bourmaud, A.; Morvan, C.; Baley, C. Elementary flax fibre tensile properties: Correlation between stress–strain behaviour and fibre composition. *Industrial Crops and Products* **2014**, *52*, 762–769. https://doi.org/10.1016/j.indcrop.2013.11.043.
86. Baley, C.; Gomina, M.; Breard, J.; Bourmaud, A.; Davies, P. Variability of mechanical properties of flax fibres for composite reinforcement. A review. *Industrial Crops and Products* **2020**, *145*, 111984. https://doi.org/10.1016/j.indcrop.2019.111984.
87. Aslan, M.; Chinga-Carrasco, G.; Sørensen, B.F.; Madsen, B. Strength variability of single flax fibres. *Journal of Materials Science* **2011**, *46*, 6344–6354. https://doi.org/10.1007/s10853-011-5581-x.
88. Barneto, A.G.; Vila, C.; Ariza, J.; Vidal, T. Thermogravimetric measurement of amorphous cellulose content in flax fibre and flax pulp. *Cellulose* **2011**, *18*, 17–31. https://doi.org/10.1007/s10570-010-9472-0.
89. Poddar, S.; Foreman, K.; Adenwalla, S.; Ducharme, S. Finite-size scaling of flexoelectricity in Langmuir-Blodgett polymer thin films. *Applied Physics Letters* **2016**, *108*. https://doi.org/10.1063/1.4939687.
90. Guiffard, B.; Saadeh, M.; Frère, P.; Seveno, R.; El-Gibari, M.; Sghaier, T.; Merupo, V.I.; Kassiba, A. Potentialities of flexoelectric effect in soft polymer films for electromechanical applications. *Journal of Physics: Conference Series* **2019**, *1322*, 012041. https://doi.org/10.1088/1742-6596/1322/1/012041.
91. Trolier-McKinstry, S., Crystal Chemistry of Piezoelectric Materials. In *Piezoelectric and Acoustic Materials for Transducer Applications*; Safari, A.; Akdoğan, E.K., Eds.; Springer US: Boston, MA, 2008; pp. 39–56. https://doi.org/10.1007/978-0-387-76540-2_3.
92. Fukada, E. Piezoelectricity as a fundamental property of wood. *Wood Science and Technology* **1968**, *2*, 299–307. https://doi.org/10.1007/BF00350276.

 doi:10.20944/preprints202506.2154.v1

93. Werling, K.A.; Hutchison, G.R.; Lambrecht, D.S. Piezoelectric Effects of Applied Electric Fields on Hydrogen-Bond Interactions: First-Principles Electronic Structure Investigation of Weak Electrostatic Interactions. *The journal of physical chemistry letters* **2013**, *4*, 1365–1370. https://doi.org/10.1021/jz400355v.
94. Werling, K.A.; Griffin, M.; Hutchison, G.R.; Lambrecht, D.S. Piezoelectric hydrogen bonding: computational screening for a design rationale. *The journal of physical chemistry. A* **2014**, *118*, 7404–7410. https://doi.org/10.1021/jp412740j.
95. García, Y.; Ruiz-Blanco, Y.B.; Marrero-Ponce, Y.; Sotomayor-Torres, C.M. Orthotropic Piezoelectricity in 2D Nanocellulose. *Scientific reports* **2016**, *6*, 34616. https://doi.org/10.1038/srep34616.
96. Nakai, T.; Hamatake, M.; Nakao, T. Relationship between piezoelectric behavior and the stress – strain curve of wood under combined compression and vibration stresses. *Journal of Wood Science* **2004**, *50*, 97–99. https://doi.org/10.1007/s10086-003-0590-2.
97. Gindl, W.; Emsenhuber, G.; Plackner, J.; Konnerth, J.; Keckes, J. Converse piezoelectric effect in cellulose I revealed by wide-angle X-ray diffraction. *Biomacromolecules* **2010**, *11*, 1281–1285. https://doi.org/10.1021/bm1000668.
98. Chae, I.; Jeong, C.K.; Ounaies, Z.; Kim, S.H. Review on Electromechanical Coupling Properties of Biomaterials. *ACS applied bio materials* **2018**, *1*, 936–953. https://doi.org/10.1021/acsabm.8b00309.
99. Abdel-karim, A.M.; Salama, A.H.; Hassan, M.L. Electrical conductivity and dielectric properties of nanofibrillated cellulose thin films from bagasse. *Journal of Physical Organic Chemistry* **2018**, *31*. https://doi.org/10.1002/poc.3851.
100. Knuffel, W.; Pizzi, A. The Piezoelectric Effect in Structural Timber. *Holzforschung* **1986**, *40*, 157–162. https://doi.org/10.1515/hfsg.1986.40.3.157.
101. Arnau, A.; Soares, D. Fundamentals of Piezoelectricity. In *Piezoelectric Transducers and Applications*; Vives, A.A., Ed.; Springer Berlin Heidelberg: Berlin, Heidelberg, 2008; pp. 1–38. https://doi.org/10.1007/978-3-540-77508-9{_}1.
102. DIN EN IEC 62631-2-1 Dielectric and resistive properties of solid insulating materials – Part 2-1: Relative permittivity and dissipation factor – Technical frequencies (0,1 Hz to 10 MHz) – AC Methods, 2018-12-00.
103. Chen, Y.C.; Lin, H.C.; Lee, Y.D. The Effects of Filler Content and Size on the Properties of PTFE/SiO 2 Composites. *Journal of Polymer Research* **2003**, *10*, 247–258. https://doi.org/10.1023/B:JPOL.0000004620.71900.16.
104. Subodh, G.; Joseph, M.; Mohanan, P.; Sebastian, M.T. Low Dielectric Loss Polytetrafluoroethylene/TeO 2 Polymer Ceramic Composites. *Journal of the American Ceramic Society* **2007**, *90*, 3507–3511. https://doi.org/10.1111/j.1551-2916.2007.01914.x.
105. Ben Amor, I.; Rekik, H.; Kaddami, H.; Raihane, M.; Arous, M.; Kallel, A. Effect of Palm Tree Fiber Orientation on Electrical Properties of Palm Tree Fiber-reinforced Polyester Composites. *Journal of Composite Materials* **2010**, *44*, 1553–1568. https://doi.org/10.1177/0021998309353961.
106. Tataroglu, A.; Durmuş, H.; Vahid, A.F.; Avar, B.; Altındal, Ş. High-temperature sensitivity complex dielectric/electric modulus, loss tangent, and AC conductivity in Au/(S:DLC)/p-Si (MIS) structures. *Journal of Materials Science: Materials in Electronics* **2024**, *35*. https://doi.org/10.1007/s10854-024-12007-7.